Electrochimica Acta 231 (2017) 171–184

Contents lists available at ScienceDirect

Electrochimica Acta

journal homepage: www.elsevier.com/locate/electacta

Research Paper

Experimental assessment and model development of cycling behavior in Li-ion coin cells

Muhammad Rashid, Amit Gupta*

Department of Mechanical Engineering, Indian Institute of Technology Delhi, New Delhi, 110016, India

ARTICLE INFO

Article history:
Received 4 October 2016
Received in revised form 23 January 2017
Accepted 7 February 2017
Available online 9 February 2017

Keywords:
Capacity fade
degradation
SEI film
gas evolution
manganese dissolution

ABSTRACT

The electrochemical performance of mesocarbon microbeads (MCMB)-lithium manganese oxide (LMO) spinel cells is examined by cyclic voltammetry, galvanostatic cycling and electrochemical impedance spectroscopy. The loss in capacity in full-cells is attributed to occurrence of parasitic reactions at the two electrodes. The contribution of each electrode in full-cell degradation is ascertained through testing of MCMB and LMO half-cells, with the former exhibiting a faster rate of degradation as compared to the latter. Lithium diffusion coefficient of MCMB and LMO electrodes are determined using the galvanostatic intermittent titration technique at various stages of cycling. The experimentally measured parameters are used to simulate the electrochemical behavior of MCMB and LMO half-cells. The computed capacity and cell potential variation show good agreement with experimentally obtained data for half-cells at 1C and 2C currents. The MCMB half-cell simulations reveal that loss in discharge capacity occurs due to thickening of SEI film, increase in gas formation and loss in cyclable lithium. Simulations of LMO half-cells show that capacity loss with cycling is a result of reduction in active material, increase in surface resistance with inactive material deposition and loss in cyclable lithium.

© 2017 Elsevier Ltd. All rights reserved.

1. INTRODUCTION

Recent advancement in Li-ion batteries (LIBs) has spurred their use in electric vehicles (EVs) and hybrid-electric vehicles (HEVs) due to their higher gravimetric and volumetric energy densities as compared to the lead-acid and nickel-cadmium batteries. However, loss in discharge capacity with repeated cycling is still a challenge for their commercialization as power sources in EVs and HEVs [1,2]. The electrochemical performance of LIBs can be improved by enhancing the discharge capacity of the anode and cathode. Researchers have focused their attention towards enhancement of battery performance in terms of energy and power density through development of new electrode materials and improving the discharge capacity and capacity retention of existing material using novel synthesis processes [3–5].

Mesocarbon microbead (MCMB) has been used as a commercial anode material due to its low redox potential, good electronic conductivity, high Li-ion mobility and great structural stability during the process of lithium intercalation and deintercalation [6–8]. However, formation of solid electrolyte interface (SEI) film due to solvent reduction during the charging process is considered as a major factor responsible for capacity reduction in MCMB anodes [9–11]. On the other hand, $LiMn_2O_4$ (LMO) spinel cathode was developed as a promising cathode material due to its ability to challenge the limitations of low abundance, higher cost and toxic nature of $LiCoO_2$ [1,2,12]. Moreover, the use of manganese oxide as cathode material minimizes safety issues and thermal runways. Due to these reasons, LMO has been projected as a suitable cathode candidate for commercialization of LIBs in EVs and HEVs [13]. Nevertheless, batteries using LMO cathode have been shown to suffer from capacity degradation due to manganese (Mn^{2+}) dissolution caused by the disproportion reaction ($2Mn^{3+} \rightarrow Mn^{2+} + Mn^{4+}$) during lithium intercalation and deintercalation in the solid matrix [13,14].

Due to repeated cycling, various side-reactions become active as the ions of lithium travel from one electrode to another through the electrolyte phase, some of which are electrolyte decomposition, passive film formation, gas evolution and active material dissolution [9,15]. These unwanted reactions consume active material and electrolytes, forming an insoluble solid, some liquid and gaseous products [16–18]. The insoluble products deposit over the electrode surface and block the pores of the electrode leading to a decreased interfacial area for electrochemical reactions. The loss of cyclable lithium due to their consumption in parasitic

* Corresponding author.
E-mail addresses: agupta@mech.iitd.ac.in, amitgupta2004@gmail.com (A. Gupta).

http://dx.doi.org/10.1016/j.electacta.2017.02.040
0013-4686/© 2017 Elsevier Ltd. All rights reserved.

Nomenclature

a_s	electrode specific interfacial area (m^{-1})
A	electrode area (m^2)
c	concentration (mol/m^3)
C	specific capacity (Ah/g)
D	diffusion coefficient (m^2/s)
E_a	activation energy (kJ/mol)
ΔE_s	potential difference between consecutive relaxations (V)
ΔE_t	potential difference incurred due to applied current (V)
F	Faraday's constant (C/mol)
$f_{\pm}$	mean molar activity coefficient
i	current (A/m^2)
i_e	ionic current (A/m^2)
J	current density (A/m^3)
k	rate constant for electrochemical reaction ($m^{2.5}/(mol^{0.5}.s)$)
k_0	dissolution reaction constant (1/s)
L	thickness (m)
m	loading of the electrode (g)
M	molecular weight (kg/mol)
n	number of electrons
n_m	moles of active material (mol)
r	particle radius (m)
R_{sei}	film resistance (Ω-m^2)
R_u	universal gas constant (J/(mol K))
t	time (s)
t_0^+	cation transference number
T	temperature (K)
U	equilibrium potential (V)
V	volume (m^3)
X_a	conversion of dissolution reaction
α_a	anodic transfer coefficient
α_c	cathodic transfer coefficient
δ_{sei}	SEI film thickness (m)
ε	volume fraction
η	overpotential (V)
κ	ionic conductivity of electrolyte (S/m)
κ_{sei}	film electronic conductivity (S/m)
ν	molar volume (m^3/mol)
σ	solid-phase electronic conductivity (S/m)
τ	time of current pulse
ϕ	potential (V)

Subscript/superscript

diss	dissolution
e	electrolyte
eff	effective
fl	filler
g	gas
int	intercalation
is	inactive solid material
n	negative electrode
ocp	open circuit potential
p	positive electrode
para	parasitic
s	solid
sd	solid deposit
sei	solid-electrolyte interface
0	initial

reaction and formation of SEI film leads to an increase in the cell impedance and is responsible for the increase in cell overpotential [19]. The formation of gas in a Li-ion battery can lead to (a) swelling and pressure build-up inside the battery, and (b) loss of contact between electrode particles and reduction in the electrolyte volume inside the porous electrode [15]. This reduction in electrolyte volume limits the diffusion of Li-ions through the electrolyte phase, thereby increasing the cell resistance and ohmic losses [20,21].

In the past, several studies have been carried out to understand the influence of electrolyte decomposition and SEI formation in carbon electrodes over capacity fading of LIBs [15–17,19–26]. These mainly include a thermo-electrochemical quasi-steady model to quantify the effect of gas evolution to observe the impact of gas volume fraction (and corresponding decrease in electrolyte volume fraction) over cell performance [15], a model for the deposition of solid from the reduction of electrolyte leading to porosity change in anode and its effect on the cycling performance of the LIBs [19], a degradation model which consider the growth of the SEI film due to the electrolyte reduction at carbon surface [23], and a model to capture the tandem effect of SEI formation and gas evolution on capacity degradation of LIBs with cycling [27].

The loss in discharge capacity with respect to cycle number due to occurrence of side-reactions at the cathode during the process of charge and discharge has also been studied by different research groups [15–17,28,29]. The commonly known side-reactions at LMO cathode are the electrolyte oxidation, manganese dissolution and Jahn-Teller distortion [9]. A model of kinetics of manganese dissolution in electrolyte caused by acid attack was used to analyze the effect of particle size on the rate of dissolution [28]. Using dissolution kinetics, a mathematical model to investigate the effect of manganese dissolution on the cycling performance of LMO cathodes under different operating voltages was also developed [29]. Some other studies have focused on capacity degradation caused by dissolution due to deposition of inactive manganese as film over the active phase [30], the effect of different kinds of side-reactions on the electrochemical performance of LMO cathode [16], and analysis of capacity degradation caused by many possible side-reactions to examine the electrochemical performance of LMO vs. graphite cells [17].

In these studies, either commercial full-cells have been analyzed whose composition and morphology were not known (or were difficult to be ascertained) or the contribution to capacity loss by each electrode could not be determined through electrochemical testing of full-cells only. Past studies have focused their attention on attributing degradation to a single electrode, and hence the benchmarking of models that capture degradation mechanisms at both negative and positive electrodes is missing. In this regard, the electrochemical characterization of MCMB and LMO half-cells and development of an experimentally validated degradation model to quantify the rate of capacity loss at each of these electrode has also not been attempted so far. It is clear that substantial effort is still required to understand physiochemical processes associated with capacity fade and degradation to improve Li-ion battery performance. Therefore, the objectives of the present work are the following:

1. Experimental assessment of cycling behavior of MCMB-LMO, Li-MCMB and Li-LMO cells to investigate their rate capability and capacity retention with cycle number.
2. Measurement and identification of cell parameters to assist in the development of an experimentally validated model for Li-MCMB and Li-LMO half-cells.
3. Numerical and experimental examination of Li-MCMB and Li-LMO half-cells to attribute the extent of cell degradation by

considering manganese dissolution, solid-electrolyte interface film formation and gas evolution as side-reactions.

With this study, we aim to ascertain the contribution of each electrode on capacity degradation of MCMB-LMO full-cells.

2. EXPERIMENTAL METHOD

2.1. Fabrication and Testing

The anode slurry was prepared by mixing MCMB (94.50 wt.%; Source: Xiamen TOB New Energy Technology, China) with carboxymethyl cellulose (CMC, 2.25 wt.%) as thickening agent, conductive graphite (1.0 wt.%) as conducting agent and styrene-butadiene rubber (SBR, 2.25 wt.%) as binder dissolved in deionized water (120 wt.%). The cathode slurry was prepared by mixing active material LMO (80 wt.%; Source: Xiamen TOB New Energy Technology, China) with polyvinylidene fluoride (PVDF, 10 wt.%) as a binder and super-P carbon black (10 wt.%) as conductive agent dissolved in N-methyl pyrrolidone (NMP) solvent (120 wt.%). The stirring process in vacuum took 3–4 hours to homogenize the slurry. The slurries prepared for anode and cathode were coated on copper (thickness of 15 μm) and aluminum (thickness of 20 μm) foils, respectively, by using film coater and doctor blade. Subsequently, the coated sheets were dried in the vacuum oven at 80 °C (anode) and 120 °C (cathode) for 12 hours to remove any traces of the liquid solvent. The thicknesses of the dried electrode sheets were reduced by a rolling press to 90% and 85% of the original thickness of the anode and cathode, respectively, to minimize the pores generated due to the evaporation of solvent and to increase the material density in the electrodes. The electrodes were characterized by using X-ray diffraction (XRD) technique and their morphology was analyzed by a scanning electron microscope (SEM). Circular disks were punched from the calendared electrodes of ϕ15 mm and separator (polypropylene film) of ϕ19 mm which were finally used to assemble the coin cells.

The 2016 type coin-cells were assembled using a crimping machine (MTI Corp.) inside a glove box (Jacomex) with moisture and oxygen concentration of less than 0.5 ppm. The electrolyte used was 1 M $LiPF_6$ dissolved as the solute in 1:1 ethylene carbonate (EC) and dimethyl carbonate (DMC). Full-cells (MCMB as negative electrode and LMO as positive electrode) were fabricated to study their electrochemical behavior. Coin cells were also assembled in half-cell (working electrode against lithium foil) format to investigate the capacity and degradation behavior of the MCMB and LMO electrodes with cycling. A battery cycler (Bio-Logic-VMP3) was used for the cyclic voltammetry, galvanostatic cycling and impedance spectroscopy of the fabricated cells.

The fabrication of full cells was done with careful consideration of material balance in order that the active material of each electrode could be optimally utilized. For a balanced cell, the ratio of its active masses (γ) was reported to be governed by the following expression [9],

$$\gamma = \frac{m_p}{m_n} = \frac{L_p \varepsilon_p \rho_p}{L_n \varepsilon_n \rho_n} = \frac{\Delta x C_n}{\Delta y C_p} \tag{1}$$

where L, ε and ρ are the thickness, porosity and density of the electrode, respectively.

In case of full-cell with MCMB as anode and LMO as cathode, the electrochemical reaction at both the electrodes with useful lithium stoichiometries of $\Delta x = 0.61$ and $\Delta y = 0.83$ [9,31–33], respectively, can be written as follows.

Anode reaction:

$$C_6 + 0.61Li^+ + 0.61e^- \underset{Discharge}{\overset{Charge}{\leftrightarrow}} Li_{0.61}C_6 \tag{2}$$

Cathode reaction:

$$LiMn_2O_4 \underset{Discharge}{\overset{Charge}{\leftrightarrow}} Li_{0.17}Mn_2O_4 + 0.83Li^+ + 0.83e^- \tag{3}$$

From the above stoichiometric electrode reactions and Eq. (1), the ratio γ of the balanced ideal cell was calculated to be 1.85. However, cells with an additional 15% of cyclic lithium were fabricated since most of the excess lithium is lost in the formation of SEI film during the 1st charging cycle. Therefore, the mass ratio of electrodes for full cell were kept to lie between 2.05-2.15.

The cells fabricated were stored (relaxed) overnight (12 hours) to allow the electrolyte to fill into the pores of the electrodes. Subsequently, electrochemical impedance spectroscopy (EIS) was conducted with a sine wave of amplitude 5 mV between frequency ranges of 20 mHz–500 kHz for the impedance measurement of fresh cells. Later, cyclic voltammetry was conducted with a scan rate of 0.1 mV/s between voltage range of 2.5-4.5 V for full-cells, 3.0-4.2 V for LMO half-cells, and 0-2.0 V for MCMB half-cells to record the redox peaks. After redox analysis, half- as well as full-cells were cycled between cut-off voltages with a constant current charge (1C or 2C), followed by constant voltage charge until the charging current decayed to C/10, and finally constant current discharge at the same rate. Fig. 1 shows the representative current and voltage profiles for all cells tested in this work. The cut-off voltages for galvanostatic cycling of Li-MCMB, Li-LMO and MCMB-LMO cells are given in Table 1. EIS of cycled cells was again performed to examine the impedance increase with cycling. Impedance at cycled stage were recorded at fully charged stage of the cell followed by a relaxation of 2 hours. The purpose of relaxation of cells was to minimize the concentration and potential gradients in the solid and electrolyte phases [34]. The SEM images of cycled electrodes were captured and compared with the micrographs of fresh electrode to observe the morphological and structural changes due to cycling of the cell.

2.2. Experimental Parameters for Mathematical Model

The experimental measurement of cell parameters was needed to conduct the computational analysis of MCMB and LMO electrodes. The electrode thickness was measured by using a micrometer and the porosity was estimated through density of the electrode (ρ_{el}) and corresponding bulk (ρ_b) density of the material by using the relation

$$\varepsilon_e = 1 - \frac{\rho_{el}}{\rho_b} \tag{4}$$

The density of the electrodes were determined by considering the effect of binders and conducting materials. The size of the electrode particles was taken from particle distribution data of the manufacturer using the D50 value which is mass median diameter

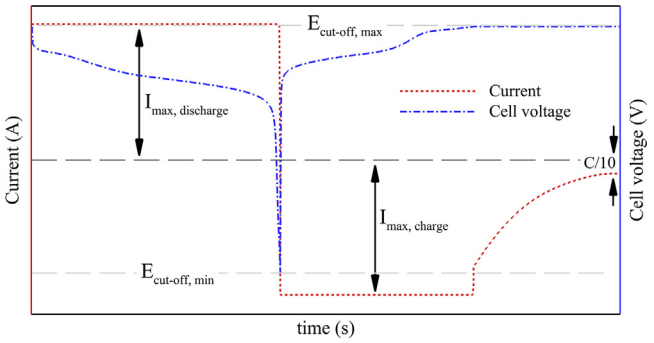

Fig. 1. Representative current and cell voltage profile for galvanostatic cycling of cells.

Table 1
Cut-off voltages used for cycling of full- and half-cells.

Cell type	Li-MCMB	Li-LMO	MCMB-LMO
Cut-off voltages (V)	0.005-2.0	3.0-4.2	3.0-4.2

of the sample. The D50 signifies the diameter at which 50% of a sample's mass is comprised of smaller particles. The filler volume that accounted for the conductive additive and binder was calculated through their bulk densities and weight fractions in the electrodes. The open-circuit potentials (OCP) of MCMB and LMO were measured by galvanostatic charging-discharging of half-cells at C/30 current and are shown in shown in Fig. 2(a) and (b). The 1C current density, defined in terms of the current which can completely discharge the cell in 1 hour, was calculated by using material loading (which were 3.17-3.24 mg/cm^2 for MCMB and 8.35-8.40 mg/cm^2 for LMO electrodes), specific capacity and area of the disk of ϕ15 mm by using the expression i_{1C} = mC/A.

An important parameter that dictates transport limitations in the active material is the diffusion coefficient of lithium in the solid phase. In order to quantify the diffusion coefficient in MCMB and LMO electrodes, galvanostatic intermittent titration technique (GITT) has been employed. In this technique, a charging current pulse of C/15 for 15 min. followed by a rest duration of 15 min. was applied on MCMB and LMO half-cells till the potential reached 0.005 V and 4.2 V, respectively. Similarly, cells were discharged with an intermittent discharge current pulse of C/15 followed by relaxation period of 15 min. till cell potential reached 2.0 V and 3.0 V, respectively. A schematic with the applied current and corresponding voltage of the half-cell is shown in Fig. 2(c). The diffusion coefficient of MCMB and LMO electrodes were calculated using the following expression [35],

$$D_{Li} = \frac{4}{\pi\tau}\left(\frac{n_m v}{A}\right)^2 \left(\frac{\Delta E_s}{\Delta E_t}\right)^2 \quad (5)$$

3. NUMERICAL METHOD

In the experimental investigations of capacity degradation of MCMB and LMO electrodes, only discharge capacity and cell impedance can be measured with respect to cycle number, and the internal increase in thickness of the SEI film, decrease in pore volume and cyclable lithium cannot be gauged through it. With this consideration, the pseudo-2D cell-scale model along with SEI formation, gas evolution and manganese dissolution as parasitic reactions was implemented to obtain a better understanding of the degradation of MCMB and LMO electrodes.

3.1. Ideal Cell Model

Newman and co-workers [31,32] first developed a mathematical pseudo-2D model for electrochemical cells using the porous-electrode theory in solid phase and concentrated solution theory for electrolyte phase with an assumption that all the electrochemical reaction take place in the cell domain are reversible in nature. The governing equations of ideal cell are discussed as follows:

In the electrolyte, the species transport is given by

$$\frac{\partial(c_e \varepsilon_{e,i})}{\partial t} = \nabla.(D_{e,i}^{eff} \nabla c_e) - \frac{i_e \cdot \nabla t_+^0}{F} + \frac{1 - t_+^0}{F} J_i \quad (6)$$

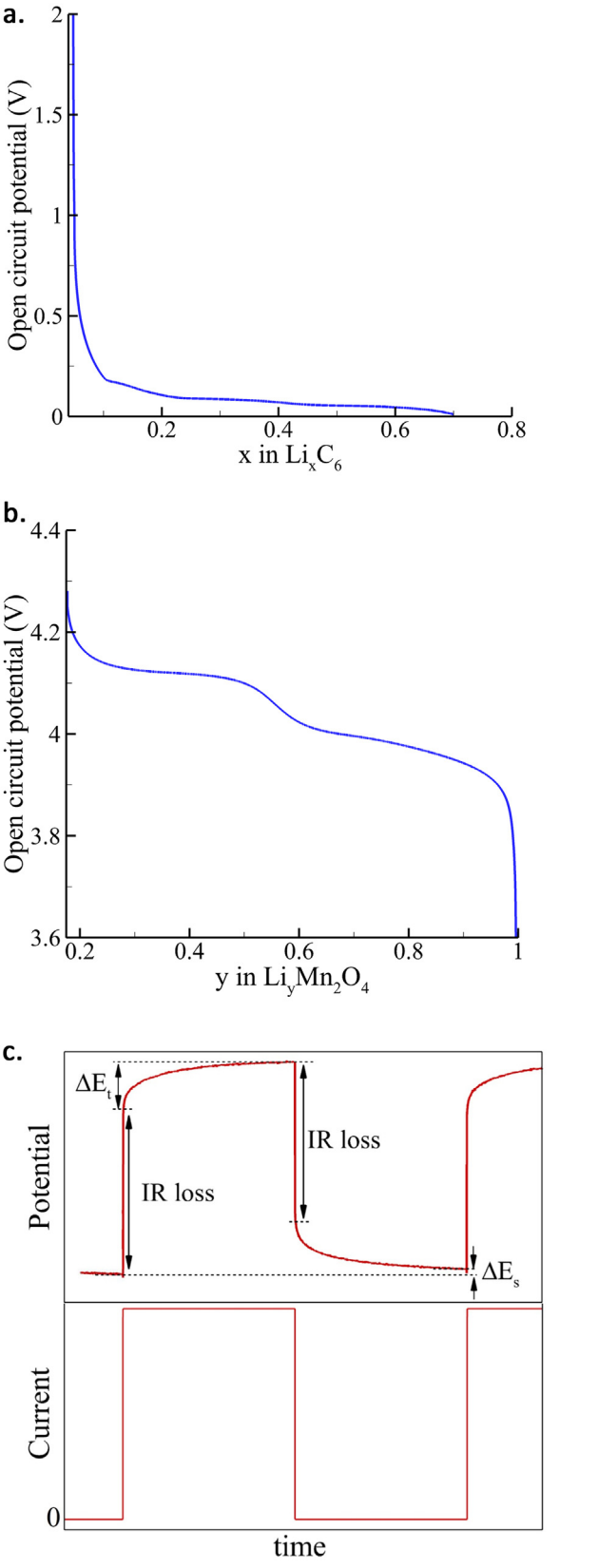

Fig. 2. Open circuit potential measured at C/30 current for (a) MCMB and (b) LMO electrodes (c) voltage and current profile for GITT.

where subscript *i* stands for negative (n) or positive (p) electrodes. The charge transport in electrolyte phase is given by

$$\nabla.(\kappa_{e,i}^{eff}\nabla\phi_e) + \nabla.\left(\frac{2R_uT\kappa_{e,i}^{eff}}{F}(t_+^0 - 1)\left(1 + \frac{d\ln(f_\pm)}{d\ln c_e}\right)\nabla\ln c_e\right) + J_i = 0 \quad (7)$$

Due to lack of experimental data, the general practice is to ignore the term $\frac{d\ln(f_\pm)}{d\ln c_e}$ in equation (7) (i.e., taken as zero) in the case of Li-ion batteries [36]. Charge transport in the solid phase is given by Ohm's law, as

$$\nabla.(\sigma_{s,i}^{eff}\nabla\varphi_{s,i}) - J_i = 0 \quad (8)$$

where J_i is given by

$$J_i = J_{int,i} \quad (9)$$

The Li-ion intercalation current density $J_{int,i}$ is given by the Butler-Volmer kinetics

$$J_{int,i} = Fa_ik_i(c_e)^{\alpha_{a,i}}(c_{s\max,i} - c_{s,i})^{\alpha_{a,i}}(c_{s,i})^{\alpha_{c,i}}(\exp\left(\frac{\alpha_{a,i}F}{R_uT}\eta_i\right) - \exp\left(-\frac{\alpha_{c,i}F}{R_uT}\eta_i\right))$$

Here, η_i represents the overpotential for intercalation reaction and is given by

$$\eta_i = \phi_{s,i} - \phi_e - U_{ocp,i} - \frac{J_i}{a_i}R_{sei,i} \quad (11)$$

It should be noted that for modeling an ideal reversible cell $R_{sei,i} = 0$. The specific interfacial area a_i of the solid phase is given by

$$a_i = \frac{3\varepsilon_{s,i}}{r_i} = \frac{3(1 - \varepsilon_{e,i} - \varepsilon_{fl,i})}{r_i} \quad (12)$$

The diffusion of lithium into the spherical particles of each electrode is governed by Fick's second law of diffusion, and is given by

$$\frac{\partial c_{s,i}}{\partial t} = D_{s,i}\frac{1}{r^2}\frac{\partial}{\partial r}\left(r^2\frac{\partial c_{s,i}}{\partial r}\right) \quad (13)$$

Finally, the effective transport properties in the electrochemical model can be correlated to intrinsic properties using the Bruggeman's relation, as

$$D_{e,i}^{eff} = D_e\,\varepsilon_{e,i}^{1.5} \quad (14)$$

$$\sigma_{s,i}^{eff} = \sigma_{s,i}\,\varepsilon_{s,i}^{1.5} \quad (15)$$

$$\kappa_{e,i}^{eff} = \kappa_e\,\varepsilon_{e,i}^{1.5} \quad (16)$$

3.2. SEI Growth and Gas Evolution Model

Electrolyte reduction is the main side-reaction at carbon electrodes that happens during charging process in which Li-ions react with the electrolyte and produce insoluble solid and gaseous products. In this work, we consider that the gas formed fills the pore volume that was earlier occupied by the electrolyte and reduces the solid-electrolyte interfacial area necessary for the electrochemical reaction. The reduction in electrolyte volume is postulated to lead to an increase in transport resistance and consequent decrease in discharge capacity of the cell. The possibility of the gas being soluble in the electrolyte is not considered in the present study due to lack of information regarding Henry's constant (Henry's law relates mole fraction of gas dissolved in liquid to partial pressure in vapor phase). In this section, the mathematical expressions to consider concurrent effect of SEI film formation and gas evolution at negative electrode due to electrolyte reduction and its coupling with pseudo-2D model has been presented.

The reduction of the electrolyte, such as ethylene carbonate (EC), at the anode is known to produce insoluble alkyl carbonates and ethylene gas [9] and is given by

$$2EC^- + 2Li^+ \rightarrow CH_2(OCO_2Li)CH_2(OCO_2Li)\downarrow + C_2H_4\uparrow \quad (17)$$

The parasitic reaction current density of the electrolyte decomposition reaction can be considered to follow the cathodic Tafel kinetics [19,23],

$$J_{para} = -a_nj_{para}^0\exp\left(-\frac{\alpha_cF}{R_uT}\eta_{para}\right) \quad (18)$$

where $j_{para}^0 = j_{1C}^0\left(\frac{i_{app}}{i_{1C}}\right)^{0.5}$ [27] and the overpotential η_{para} can be written as

$$\eta_{para} = \phi_{s,n} - \phi_e - U_{para} - \frac{J_n}{a_n}R_{sei} \quad (19)$$

where $J_n = J_{int,n} + J_{para}$

The fractional volume of solid deposit (in the form of SEI film) and gases produced by electrolyte decomposition reaction at anode can be written as [16]

$$\frac{\partial\varepsilon_j}{\partial t} = -\frac{J_{para}v_j}{nF} \quad (20)$$

where subscript j stands for solid deposit (sd) and gas (g).The thickness of the SEI film can be expressed as [27]

$$\delta_{sei,n} = r_{s,n}\left[\left(1 + \frac{\varepsilon_{sd}}{\varepsilon_{s,n}}\right)^{1/3} - 1\right] \quad (21)$$

The SEI film resistance ($R_{sei,n}$) is given as

$$R_{sei,n} = \frac{\delta_{sei,n}}{\kappa_{sei,n}} \quad (22)$$

The instantaneous electrolyte volume fraction due to film formation and gas generation is given by

$$\varepsilon_{e,n}(t) = \varepsilon_{e,n}^0 - \varepsilon_{sd} - \varepsilon_g \quad (23)$$

3.3. Manganese Dissolution Model

Manganese dissolution in the electrolyte is considered to be the main side-reaction responsible for capacity degradation in spinel electrode which takes place due to acid attack and disproportion reaction at cathode [9,28]. The dissolution of Mn^{3+} takes place according to the following reaction [30]:

$$2Mn^{3+}(s) \rightarrow Mn^{4+}(s) + Mn^{2+}(l) \quad (24)$$

The manganese dissolution in the electrolyte is governed by [28]

$$1 - (1 - X_a)^{1/3} = kt \quad (25)$$

where the rate of dissolution reaction (k) depends on the reaction temperature and activation energy by $k = k_0\exp(-E_a/RT)$ [28] and $k_0 = k_{1C}\left(\frac{i_{app}}{i_{1C}}\right)^{0.5}$ is assumed.

The volume fraction of the active material decreases with the dissolution of manganese in the electrolyte. Therefore, the

remaining active material ($\varepsilon_{s,p}$) can be expressed as [30]

$$\varepsilon_{s,p} = \varepsilon^0_{s,p}\frac{1}{1+X_a} \tag{26}$$

Using this, the instantaneous radius ($r_{s,p}$) of the active particle can be calculated by [30]

$$r_{s,p}(t) = \left(\frac{1}{1+X_a}\right)^{1/3} r^0_{s,p} \tag{27}$$

The film resistance ($R_{sei,p}$) due to inactive deposition is expressed as [30]

$$R_{sei,p} = \frac{r^0_{s,p}}{\kappa_{sei,p}}\left(\left(\frac{1+0.75X_a}{1+X_a}\right)^{1/3} - \left(\frac{1}{1+X_a}\right)^{1/3}\right) \tag{28}$$

and the instantaneous porosity of the cathode can be written as [30]

$$\varepsilon_{e,p} = 1 - \varepsilon^0_{s,p}\frac{1+0.75X_a}{1+X_a} - \varepsilon_{f,p} \tag{29}$$

3.4. Solution Technique

The set of governing equations with SEI formation and gas evolution model were implemented to quantify the electrochemical performance of Li-MCMB cell. For Li-LMO cells, ideal cell and manganese dissolution model expressions were solved to study the degradation behavior of these half-cells with cycling. The finite-element based COMSOL Multiphysics toolkit has been used for conducting simulations with a time step of one second and convergence limit of 10^{-3}. The size of elements was chosen in such a way to obtain grid independent results. To keep the analysis realistic, model input parameters were measured through experiments, whenever possible, with a few taken from the literature. The degradation parameters of LMO (k_0) and MCMB (j^0_{1C}) were chosen to achieve satisfactory agreement with measured and computed half-cell capacities for N = 1 and 100 cycles. The reaction constants for the intercalation electrochemical reaction (k_i) were determined such that the computed cell potential imitated the experimentally measured value for the first discharge-charge cycle. It should be noted that these parameters are not universal and may change depending on the differences in the electrode fabrication processes, electrode composition (% additives), the choice of the electrolyte and the type of the cell (coin, prismatic, pouch). Yet, the advantage of this model is that it demonstrates that the degradation route can be accurately captured by the mechanisms considered herein instead of focusing on various other possibilities that have been listed in earlier publications. The current profile was identical to that used in experiments. The transport properties of electrolyte (1 M $LiPF_6$ in 1:1 EC:DMC) used in the simulations are given as [37]

$$D_e = 5.34 \times 10^{-10} e^{-0.65(c_e/1000)} \tag{30}$$

$$\kappa_e = 0.0911 + 1.9101\left(\frac{c_e}{1000}\right) - 1.052\left(\frac{c_e}{1000}\right)^2 + 0.1554\left(\frac{c_e}{1000}\right)^3 \tag{31}$$

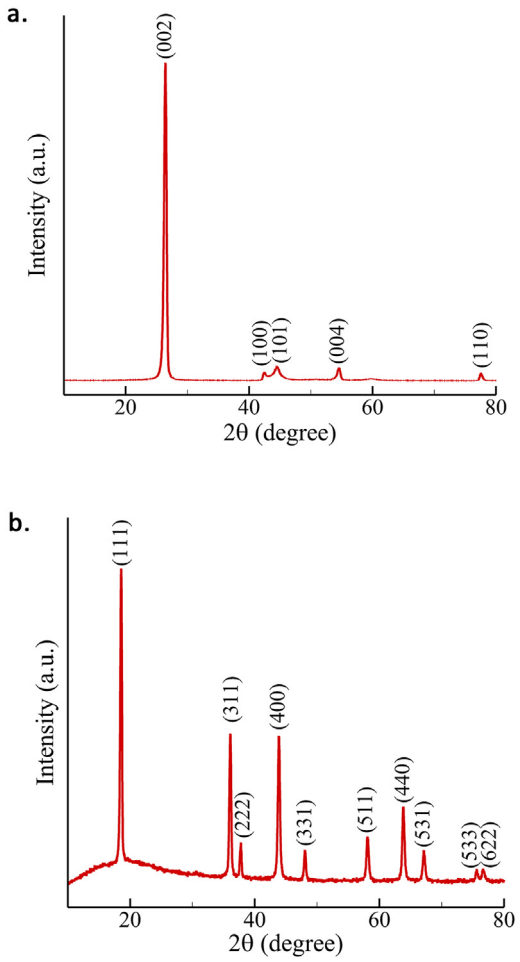

Fig. 3. X-ray differaction pattern of (a) MCMB and (b) LMO electrodes.

4. RESULTS AND DISCUSSION

4.1. Characterization

Structural characterization of MCMB and LMO electrodes was carried out to ascertain the crystal structure of the material by using the XRD technique. Fig. 3(a) shows the XRD pattern indicating the characteristics peaks at various diffraction angles of the MCMB electrode. A strong intensity narrow peak at diffraction angle of 26.5° ($2\theta = 26.5°$) is observed which corresponds to Miller indices of (002), confirming that the sample material is graphitized carbon with high crystallinity, i.e., MCMB. The lattice spacing analogous to Miller indices of (002) is 3.35 Å [8,38,39] which also signifies towards sample material as graphitized carbon.

The XRD characteristic peaks obtained through diffracted incident beams by the planes of the LMO material at different diffraction angles (2θ), is shown in Fig. 3(b). All the peaks in this spectrum are sharp and well defined, signifying the fine crystallinity of LMO without any additional peak to indicate impurity in the material. From these characteristics peaks, it can be identified that the sample material is single-phase spinel structure with a space group Fd3m (which agreed with JCPDS card No. 35-0782) [40]. In this structure, Li-ions take tetrahedral sites (8a), Mn-ions occupy octahedral (16d) sites and oxygen ions are located at the 32e sites of the frame [41,42].

4.2. MCMB-LMO Full-cells

After conducting structural and morphological analysis of fresh electrodes, coin cells of 2016-type were assembled with MCMB and LMO as anode and cathode, respectively. As a representative case, the redox kinetics of a particular MCMB-LMO full cell fabricated with mass ratio of 2.09 has been presented in Fig. 4(a) using cyclic voltammogram obtained by subjecting the cell to a voltage ramp between 2.5-4.5 V at a scan rate of 0.1 mV/s. In this CV plot, two pairs of redox peaks are observed which confirm the two distinct oxidation states of Mn in spinel LMO. Comparing the I–V profile at different cycles shows that the area under the 1st cycle anodic peak is much higher than the succeeding cycles. However, the first cathodic scan only has marginally higher area under the curve, which evidently shows higher capacity loss during first lithiation of the MCMB that is caused by the loss of lithium in the formation of the initial SEI film [9]. The reduced irreversible capacity loss in subsequent cycles is due to the lower availability of the surface area at anode for the electrolyte reduction during charging process of the cell.

To differentiate between the cyclic voltammograms of Li-LMO and MCMB-LMO cells, the CV plot of Li-MCMB cells shown in Fig. S1 (supplementary material) can be observed to exhibit the lithiation and delithiation potentials of 0.036 and 0.285 V, respectively. The peak voltages of delithiation and lithiation of LMO electrodes against Lithium foil and MCMB as anodes are also shown in Fig. S2 (supplementary material). By comparing the redox peaks of the Li-LMO and MCMB-LMO cells, a shift in peak voltages in the latter case is observed which is attributed to the presence of MCMB as anode. Due to the insertion resistance experienced by Li-ions in MCMB anode, the cell irreversibility increases which is also noticeable from the change in potential as shown in Fig. S2.

Fig. 4(b) shows the variation of discharge capacity with respect to cycle number of cells cycled at 1C-rate and 2C-rate between 3.0-4.2 V. To conduct this test, balanced cells were fabricated with γ of 2.06, 2.09, 2.07 and 2.08 for cell 1, 2, 3 and 4, respectively, with the initial capacities of the four cells ranging between 1.07-1.11 mAh. The three cells cycled at 1C-rate exhibit good repeatability in data for 100 cycles. The capacity is shown to be decreasing monotonously with cycling. The loss in cell capacity is determined to be 23-25% after cycling the cells for 100 cycles at 1C-rate. From Fig. 4(b), it is also observed that the rate of capacity loss is higher in case of cells cycled at 2C current which is expected to be caused by increased kinetic and concentration polarization (due to transport limitations in the solid matrix of the electrodes). At 2C-rate, the initial discharge capacity was measured to be 1.00 mAh with 37.5% loss in capacity after 100 cycles. Clearly, the capacity loss depends on the rate of cycling with a greater degradation observable for higher rate.

The variation in cell voltage as a function of discharge capacity at different stages of cycling at 1C and 2C-rates is shown in Fig. 4(c). The cell capacity is observed to be 1.00 and 0.63 mAh for 2C current as compared to 1.08 and 0.83 mAh at 1C current for the 1st and 100th cycle, respectively. Comparing the cell potential at discharge phase of 1st cycle shows a lower plateau voltage in case of cell cycled at 2C current. Moreover, the drop in plateau voltage with cycling is rapid for 2C-rate expectedly due to an increased overpotential and transport limitations.

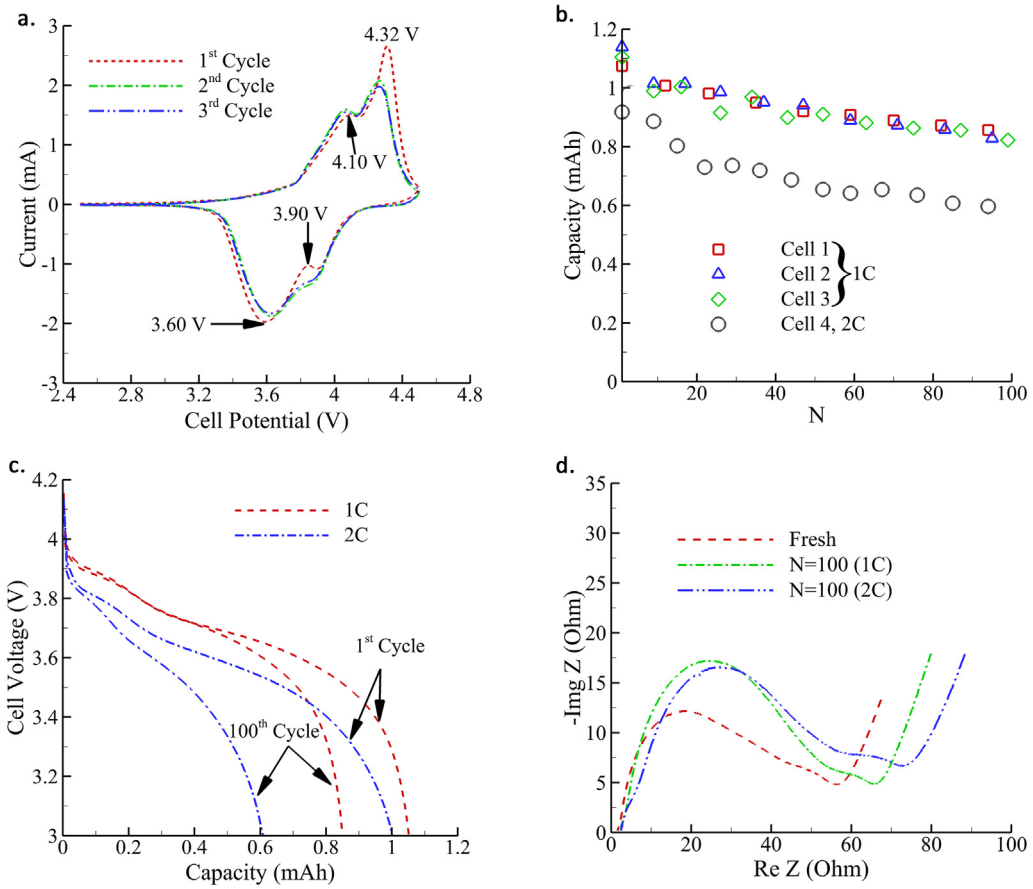

Fig. 4. Electrochemical performance of LMO-MCMB cells obtained through experiments showing results of (a) cyclic voltammogram at scan rate of 0.1 mV/s, (b) discharge capacity vs. cycle number, (c) 1st and 100th cycle cell potential vs. discharge capacity and (d) impedance spectra at fresh and after 100 cycles at 1C and 2C-rates.

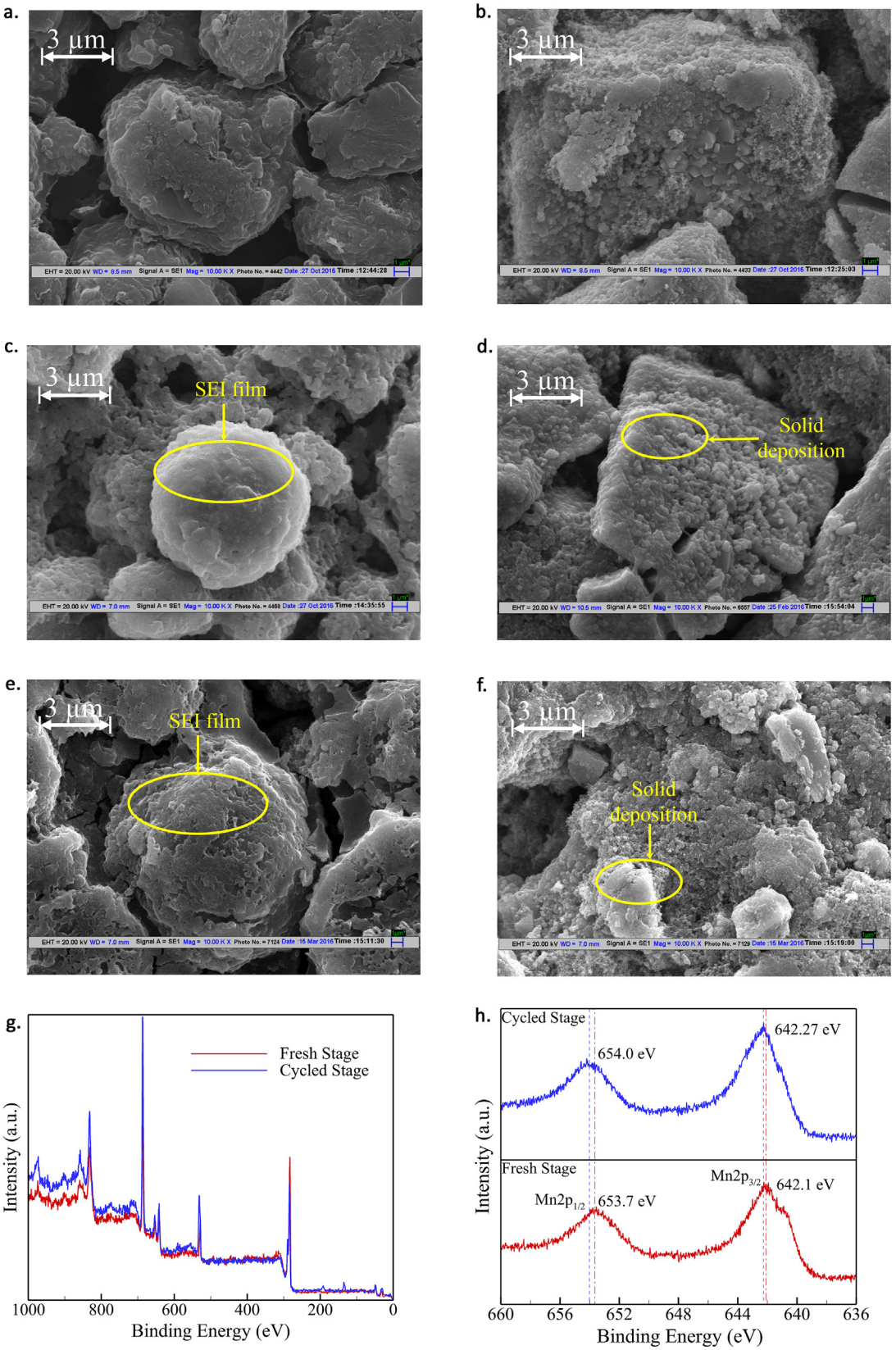

Fig. 5. SEM images of the electrodes (a) fresh MCMB, (b) fresh LMO, (c) MCMB and (d) LMO cycled at 1C-rate, and (e) MCMB and (f) LMO cycled at 2C-rate (g) XPS spectra of fresh and cycled LMO electrode and (h) comparison of Mn peaks at fresh and cycled stage.

To demonstrate the effect of parasitic reaction on the loss in cell capacity, Fig. 4(d) shows the cell impedance (conducted at OCP of 4.2 V) at fresh and 100th cycle for cell 1 and cell 4 cycled at 1C and 2C-rates, resepectively. This plot demonstrates that with an increase in cycle number cell impedance also increases due to the deposition of solid precipitates and gaseous products from the parasitic reactions. The change in electrode porosity and formation of gases reduces the solid-electrolyte contact area which leads to lowered discharge capacity of the cell. From these profiles, it can also be observed that the impedance increases at a faster rate in case of cells cycled at 2C current which is responsible for faster capacity loss at higher currents. Moreover, the capacity loss of cell at higher discharge rates are also caused by increased kinetic overpotential, IR losses and diffusion limitations of lithium in the solid phase of the battery.

Fig. 5(a) and (b) show the fresh stage micrographs of MCMB and LMO electrodes, respectively. The SEM micrograph in Fig. 5(a) was also used to verify that the average particle size of MCMB lay between Φ10–14 μm, which matched the manufacturer specifications of particle distribution with average size (D50) of 11.50 μm [43]. For LMO, the fresh electrode exhibits fine crystallinity of cubic spinel structure with particle of Φ20–22 μm (see Fig. 5(b)) which as per the manufacturer's specification is expected to lie between Φ4–40 μm [43].

After galvanostatic cycling, cells were disassembled in the glove box, electrodes dried in the vacuum oven and their SEM images were captured. In order to observe the changes in the surface morphology due to magnitude of cycling current, the SEM micrographs of these electrodes are shown with the images of fresh electrode. Figs. 5(c)-5(f) show the images of the cathodes and anodes of the cells cycled at 1C and 2C currents for 100 cycles. By comparing the images of fresh and cycled electrodes, the deposition of the solid precipitates on active material particles can be clearly inferred. In case of LMO electrode, inactive Mn^{4+} is expected to deposit over the reactive surface, while in MCMB electrode, graphite is covered with the SEI layer whose thickness increases with cycling.

The change in the oxidation state of Mn in spinel electrode due to occurrence of disproportionation reaction was investigated by conducting X-ray photoelectron spectroscopy (XPS) of LMO samples at fresh and cycled stage. The XPS spectra of fresh and cycled electrodes and a comparison of Mn($2p_{3/2}$) and Mn($2p_{1/2}$) peaks is shown in Fig. 5(g) and 5(h), respectively. The Mn($2p_{3/2}$) peak is identified at the binding energy of 642.10 and 642.27 eV for the former and latter case, respectively. Moreover, a small shift and broadening of peak towards increasing binding energy is noticeable which can be attributed to the rise in oxidation state of the Mn ions in the cycled sample [44]. To quantify the composition of oxidation states in LMO, the Mn($2p_{3/2}$) peak was deconvoluted into two peaks corresponding to Mn^{3+} at 641.5 eV [45] and Mn^{4+} at 642.7 [45] eV (shown in Supplementary material as Fig. S3(a) and S3(b) for fresh and cycled electrodes, respectively). Using area under the curve of fitted peaks, the compositional analysis of a fresh sample was determined to be 49.7 and 50.3% for Mn^{3+} and Mn^{4+}, respectively. The same procedure when applied for the electrode discharged to 100 cycles gave the composition of the surface layer as 38.8 and 61.2% of Mn^{3+} and Mn^{4+}, respectively. This characterization supports the claim of deposition of Mn^{4+} ions in the form of MnO_2 over the reactive surface of the spinel electrode which increases the cell resistance. The amount of MnO_2 deposition is expected to increase with cycling leading to further capacity degradation of LMO electrodes.

The electrochemical behavior of MCMB-LMO full-cells was presented so far to categorize the capacity degradation with cycling at 1C and 2C current. However, the loss in discharge capacity in cycling of full-cells are the cumulative effect associated with the MCMB and LMO electrodes and the contribution of each electrode in capacity fade cannot be individually acknowledged. Moreover, the identification of electrode which plays a dominant role in rapid capacity loss also cannot be done in full-cells. With this consideration, MCMB and LMO half-cells were fabricated with similar loading of the electrode as it was in full-cells and electrochemical degradation behavior with cycling at 1C and 2C current (similar with full-cells) was examined and is presented in the following sub-sections.

Table 2
Diffusivity measurements for MCMB and LMO electrodes performed using GITT.

	State of lithiation	Lithium diffusivity (m^2/s)					
		N = 1		N = 50		N = 200	
		Charge	Discharge	Charge	Discharge	Charge	Discharge
MCMB	0	3.98×10^{-13}	3.38×10^{-13}	3.76×10^{-13}	1.89×10^{-13}	2.97×10^{-13}	8.46×10^{-14}
	0.1	1.89×10^{-14}	1.07×10^{-14}	5.12×10^{-14}	1.42×10^{-13}	7.10×10^{-14}	1.49×10^{-13}
	0.2	3.24×10^{-14}	2.01×10^{-14}	4.00×10^{-14}	4.19×10^{-14}	6.84×10^{-14}	5.33×10^{-14}
	0.3	3.66×10^{-16}	1.45×10^{-14}	8.63×10^{-16}	3.37×10^{-14}	2.15×10^{-15}	3.70×10^{-14}
	0.4	5.62×10^{-16}	8.35×10^{-16}	2.54×10^{-15}	1.30×10^{-14}	1.25×10^{-14}	5.15×10^{-14}
	0.5	3.37×10^{-15}	7.51×10^{-16}	1.72×10^{-14}	1.50×10^{-15}	1.09×10^{-14}	1.09×10^{-14}
	0.6	2.67×10^{-15}	1.36×10^{-14}	3.58×10^{-16}	3.27×10^{-15}	5.77×10^{-16}	4.73×10^{-15}
	0.7	8.23×10^{-17}	1.20×10^{-15}	4.02×10^{-16}	3.95×10^{-14}	2.88×10^{-15}	4.71×10^{-14}
	0.8	2.97×10^{-16}	1.95×10^{-16}	1.17×10^{-15}	1.49×10^{-15}	4.55×10^{-15}	5.57×10^{-15}
	0.9	3.18×10^{-15}	5.63×10^{-16}	8.45×10^{-15}	7.85×10^{-16}	8.97×10^{-15}	3.21×10^{-15}
	1	5.27×10^{-14}	1.15×10^{-13}	4.87×10^{-14}	1.52×10^{-14}	2.56×10^{-14}	6.94×10^{-15}
LMO	0	2.02×10^{-13}	8.48×10^{-14}	2.17×10^{-13}	1.57×10^{-13}	2.27×10^{-13}	5.23×10^{-14}
	0.1	1.22×10^{-13}	8.88×10^{-14}	1.30×10^{-13}	1.07×10^{-13}	9.44×10^{-14}	1.83×10^{-13}
	0.2	9.44×10^{-14}	5.57×10^{-14}	9.50×10^{-14}	6.92×10^{-14}	5.44×10^{-14}	9.08×10^{-14}
	0.3	6.94×10^{-14}	4.04×10^{-14}	7.90×10^{-14}	5.20×10^{-14}	4.37×10^{-14}	6.72×10^{-14}
	0.4	5.44×10^{-14}	2.68×10^{-14}	5.24×10^{-14}	2.80×10^{-14}	3.45×10^{-14}	4.39×10^{-14}
	0.5	1.66×10^{-13}	1.17×10^{-13}	1.21×10^{-13}	9.90×10^{-14}	7.37×10^{-14}	9.00×10^{-14}
	0.6	1.39×10^{-13}	9.63×10^{-14}	1.54×10^{-13}	1.45×10^{-13}	1.11×10^{-13}	1.48×10^{-13}
	0.7	3.35×10^{-14}	1.90×10^{-14}	6.70×10^{-14}	4.27×10^{-14}	3.54×10^{-14}	6.07×10^{-14}
	0.8	7.19×10^{-15}	4.48×10^{-15}	1.66×10^{-14}	7.24×10^{-15}	9.15×10^{-15}	1.26×10^{-14}
	0.9	2.87×10^{-14}	3.44×10^{-14}	5.09×10^{-14}	3.00×10^{-14}	3.19×10^{-14}	3.37×10^{-14}
	1	1.10×10^{-13}	9.25×10^{-14}	1.19×10^{-13}	5.84×10^{-14}	4.00×10^{-14}	7.15×10^{-14}

4.3. Model Parameters of Li-MCMB and Li-LMO Cells

The lithium diffusion coefficients $D_{Li,MCMB}$ and $D_{Li,LMO}$ of MCMB and LMO, respectively, computed at different states of lithiation during the charging and discharging processes of 1st, 50th and 200th cycle using GITT are listed in Table 2. Fig. S4(a) and S4(b) show the variation of cell potential with time recorded by applying intermittent current during process of charge and discharge of MCMB and LMO electrodes, respectively. These charging and discharging profiles were used to identify the lithium diffusivity during lithiation and delithiation of MCMB and LMO electrodes. The ΔE_s and ΔE_t values recorded from potential plateaus at different state of lithiation were employed in Eq. (5) for the quantification of lithium diffusivity in these electrodes. Form this data it can be observed that the diffusivity for MCMB and LMO varies between 1.95×10^{-16} to 3.98×10^{-13} m^2/s and 9.15×10^{-15} to 2.27×10^{-13} m^2/s, respectively, with state of lithiation (defined as fraction of experimentally obtained cycle capacity). The large variation is expected to be caused by the lattice deformation due to Li-ions extraction and insertion in the electrodes [46–48]. For MCMB, the diffusion coefficient increases by a few orders of magnitude in case of 0 and 1.0 state of lithiation in charging and discharging phase as compared to 0.1-0.9. The measured values of diffusivity are in good agreement with the data reported in literature where it has been shown that the Li-ion diffusivity in MCMB electrode varies between 10^{-17} to 10^{-13} m^2/s [46]. For LMO, the variation in diffusivity with state of charge is consistent with the data earlier reported [49] with the maximum and minimum value at the 0 and 0.8 state of lithiation found to be in good agreement with the diffusivities estimated in earlier studies [48,50]. In addition, the reported diffusivity also has a local maximum at intermediate state of lithiation, which is identical in case of both processes, i.e., charging and discharging.

As shown in Table 2, the lithium diffusion coefficient varies between 10^{-13}-10^{-16} and 10^{-13}-10^{-15} m^2/s for MCMB and LMO electrodes, respectively. Implementing such a variation of diffusion coefficient with state of lithiation and cycle number into a numerical model was found to be a challenging task. To reduce model complexity, numerical simulations were conducted with a fixed diffusivity value which captured the trends in the degradation behavior of these half-cells with cycling. The final list of parameters along with values which were employed to conduct the numerical simulations of Li-MCMB and Li-LMO half-cells are listed in Table 3.

Table 3
Parameters used in numerical simulation of MCMB and LMO half-cells.

Symbol	MCMB	LMO	Separator
L (m)	27×10^{-6} [a]	55×10^{-6} [a]	25×10^{-6} [a]
D_s (m^2/s)	3.9×10^{-14} [a]	1×10^{-14} [a]	
r (m)	6×10^{-6} [a]	8×10^{-6} [a]	
ε_e	0.285[a]	0.493[a]	
ε_{fl}	0.005[a]	0.20[a]	
σ (S/m)	100[b]	3.8[b]	
c_e^0(mol/m3)	1000	1000	1000
$c_{s\ max}$(mol/m^3)	30555[b]	22860[b]	
c_s^0(mol/m3)	17216 [c]	3900 [c]	
k_i ($m^{2.5}$/(mol$^{0.5}$.s))	4.5×10^{-12} [d]	5×10^{-11} [d]	
α_a, α_c	0.5[b]	0.5[b]	
t^+	0.363[b]	0.363[b]	0.363[b]
T (K)	303	303	
1C (A/m^2)	9.88	9.88	
U_{para} (V)	0.38[b]		
κ_f (S/m)	3.79×10^{-7} [b]	1×10^{-5} [c]	
M (kg/mol)	0.1[b]		
ρ_{para}(kg/m^3)	2.3×10^3 [b]		
j_{1C}^0(A/m2)	1.35×10^{-7} [d]		
$k_{0,1C}$ (1/s)		6.35×10^5 [d]	
E_a (kJ/mol)		72.84[b]	

[a]Measured, [b]from Refs. [26,29,30,33],[c]assumed and d fitted.

4.4. Li-MCMB Half-cells

MCMB half-cells were fabricated against Li-metal anode and their electrochemical performance assessment was carried out through galvanostatic cycling and EIS. The discharge capacity of the MCMB half-cells was analyzed by application of current at 1C and 2C-rates between the cut-off voltages of 0.005-2.0 V. Fig. 6(a) shows a comparison of the variation of discharge capacity with cycle number obtained through experiments and simulations for the MCMB half-cells cycled at 1C and 2C-rates for 100 cycles. The simulated results are in good agreement with experimental findings and demonstrate a gradual decrease in capacity as the cycle number increases. The first cycle discharge capacity was quantified to be 1.56 and 1.51 mAh for 1C and 2C rates, respectively. The loss in capacities are observed to be 37.79 and 46.40% of the initial capacity in 100 cycles for 1C and 2C currents, respectively.

The simulated and measured cell potential variations with discharge capacity for 1st and 100th cycle for 1C and 2C-rates are shown in Figs. 6(b)-6(c) and compare well with each other. The simulated 2C profile for 100th cycle deviates from the experiments near the low capacity end due to the increased ohmic overpotential accounted by the model at high currents. A higher plateau voltage is also observed due to increased cell overpotential in case of cycling at 2C rate. The rise in transport limitations as a result of cycling can be observed by inspection of the voltage plateaus at 1st and 100th cycle for 1C rate as is shown in Fig. 6(b). Similar to 2C rate, the voltage plateau exhibits a shift with increasing cycle number in case of 1C current as well though it is not as significant. As described in an earlier section, the model parameters were determined by comparing experimental capacities with simulation predictions at 1C rate only. Such a fitting was not employed to obtain model response when cycling at 2C rate; rather the same parameters were used. As a result, limitations associated with Bruggeman's relation (equations (14)–(16)) and unknown parasitic reactions that may activate at high currents could possibly be the reasons for the deviation in voltage profiles at 2C current and would be focus of a forthcoming work.

The EIS technique was employed in order to study the rise in cell impedance due to irreversible side-reactions at fresh and after 100 cycles of cells cycled at 1C and 2C rates. The impedances measured at fully charged state of MCMB electrode at 0.005 V for both currents are presented in Fig. 6(d). This plot clearly shows a rise in cell impedance at higher rate cycling. This increase in cell impedance has been postulated to be caused by carbonate deposition on the active material and gas formation and is responsible for the capacity fade with cycling of the cell. In addition, the shift in high frequency intercept in the impedance spectra is possibly due to irregular surface deposition of lithium over metallic lithium and reduction in pore volume due to SEI formation in MCMB electrode.

This loss in capacity is further examined through lithium concentration, growth in SEI film resistance and gas formation in the electrode obtained from numerical simulations. The cause of degradation of MCMB half-cells can be explained by using Table 4 which shows the decrease in electrode porosity and increase in cell resistance due to occurrence of electrolyte decomposition reaction at the electrode. The reduction in porosities are quantified to be 6.01 and 8.18% of the electrode volume at 1C and 2C currents,

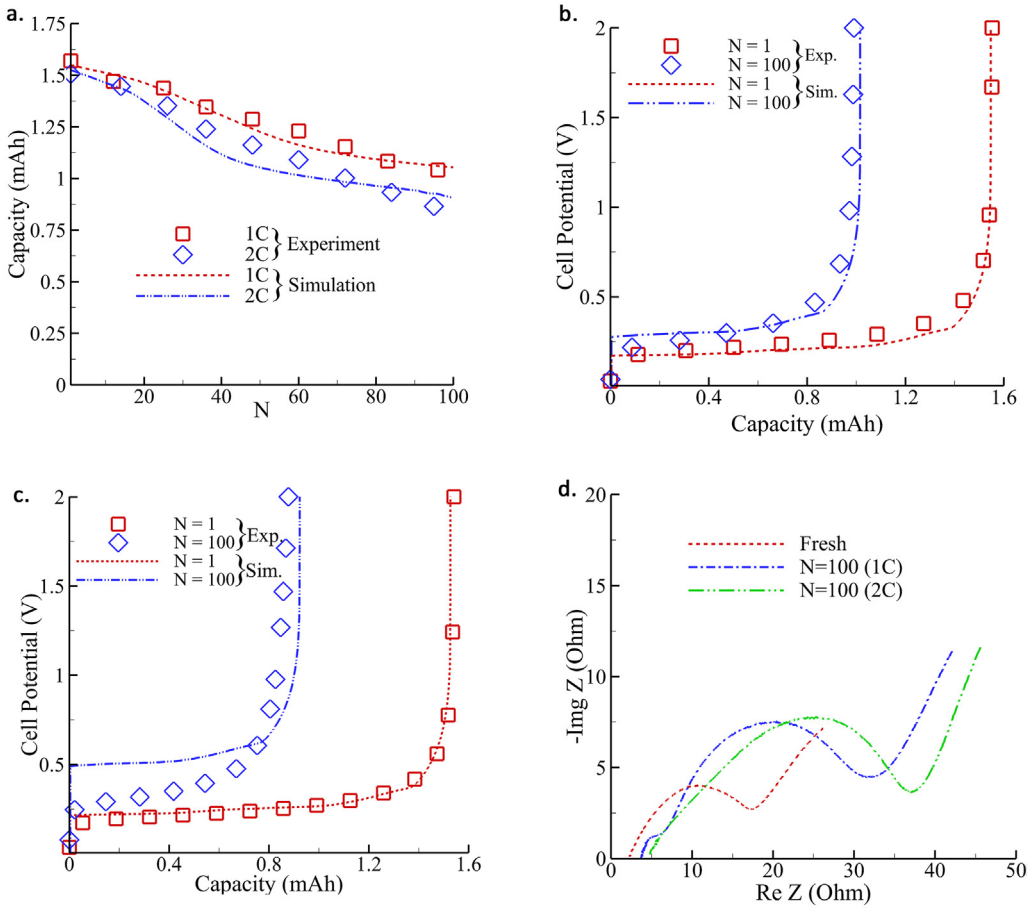

Fig. 6. Electrochemical assessment of Li-MCMB cells (a) cycling performance at 1C and 2C current, 1st and 100th cycle cell potential vs. discharge capacity at (b) 1C and (c) 2C rates (d) impedance spectra at fresh and 100th cycles at 1C and 2C rates.

Table 4
Various properties of MCMB half-cells predicted by simulations at different stages of cycling.

Rate	N	ε_e	ε_g	R_{sei} (Ω-m^2)	C_s (M) at EOC	C_s (M) at EOD
1C	1	0.283	0.001	0.003	19.963	1.804
	50	0.247	0.031	0.058	15.706	1.805
	100	0.224	0.049	0.093	13.669	1.805
2C	1	0.284	0.001	0.002	20.001	2.156
	50	0.237	0.039	0.073	14.477	2.157
	100	0.209	0.062	0.116	12.927	2.158

respectively, which is occupied by the evolved ethylene gas and deposition of solid precipitates from the parasitic reaction and leads to lower electrode-electrolyte interfacial area available for the ensuing electrochemical reactions. Moreover, the deposition of lithium ethylene carbonate as the solid precipitate is shown to increase the film resistances to 0.093 and 0.116 Ω-m^2 in 100 cycles at these currents, which physically results in increased diffusional resistance for lithium intercalation and deintercalation in the solid matrix. The variation of average lithium concentration in the solid active phase is also examined to observe the effect of repeated cycling on its amount stored in the MCMB electrode. The space averaged lithium concentration at end of charge (EOC) for different cycles of cell cycled at 1C and 2C currents is also listed in Table 4. From this data, it can be noticed that the concentration of lithium gradually decreases at EOC with relatively faster rate at 2C current while concentration at end of discharge (EOD) is nearly uniform. Therefore, the loss of cyclable lithium is concluded to increase at a higher rate at 2C current. Along with rise in cell resistance and reduction in porosity and interfacial area of the MCMB electrode, the loss in cyclable lithium is also contributing to loss in cell capacity with cycling.

4.5. Li-LMO Half-cells

The electrochemical performance evaluation of LMO, similar to the one conducted for the MCMB electrode, was also carried out. The active material loading of electrode was identical as it was in full cells and the protocols followed to quantify capacity were consistent for the sake of comparison of loss in discharge capacity with cycling. Fig. 7(a) shows the experimentally and numerically obtained capacity derived from cycling 2016 LMO coin cells at 1C and 2C rates for 100 cycles. The experimental and simulated results are in excellent agreement, indicating that the capacity decreases gradually as cycle number increases. The first cycle capacities are measured to be 1.29 and 1.09 mAh at 1C and 2C, respectively, with 16.5% and 22.0% loss in initial capacity after 100 cycles. This loss in capacity, which we regard as having been caused by Mn^{2+} dissolution in electrolyte, induces a reduction in volume fraction of solid matrix of LMO cathode. In addition, manganese (Mn^{4+}) is theorized to be deposited as inactive phase over the active particle of the electrode, thereby increasing Li-ion intercalation and deintercalation resistance, which are assumed to be factors responsible for degradation of the spinel material.

The experimentally and numerically derived cell potential vs. discharge capacity curves for 1st and 100th cycles at 1C and 2C currents are compared in Fig. 7(b) and 7(c), respectively. The

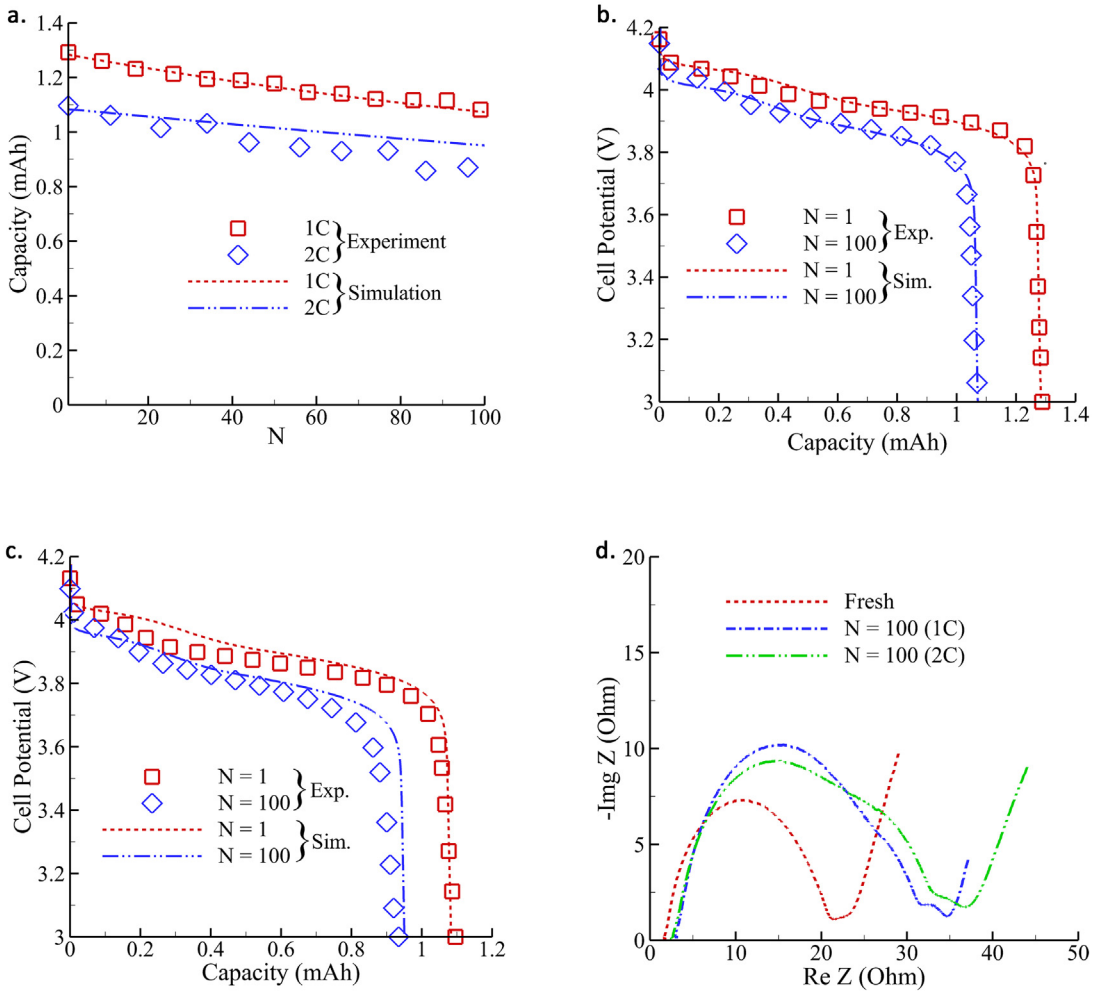

Fig. 7. Electrochemical assessment of Li-LMO half-cells with (a) cycling performance at 1C and 2C current, 1st and 100th cycle cell potential vs. discharge capacity at (b) 1C and (c) 2C-rates (d) impedance spectra at fresh and 100th cycles at 1C and 2C-rates.

simulated results are in excellent agreement with measured data for both C-rates. The potential profile at 1C current shows two different plateaus corresponding to the different oxidation states of the manganese in the spinel cathode. With further cycling, the plateau potential decreased and approached a single plateau as is shown in Fig. 7(b). The discharge profile at 2C current is shown to have lower plateau of cell voltage (see Fig. 7(c)) as compared to 1C, which is due to the increased IR losses in the cell cycled at this current. Moreover, it is also observed that as the cycle number increases the plateau voltage decreases with increasing current, which is also an evidence of the increase in cell overpotential and voltage drop due to the reduction in active material volume fraction. The cell potential obtained during discharge at high current shows steep decay and reaches the lower cut-off voltage at much lower capacity.

EIS tests were conducted for the half-cells after they reached a potential of 4.2 V by providing a relaxation for 2 hours at the end of 1st and 100th charging cycles. The impedance spectrum is shown in Fig. 7(d) through which the loss in discharge capacity with increase in cycle number can also be understood. This impedance plot highlights the increase in magnitude of the solvent, lithium migration and charge transfer resistances (shown by the increase in radius of semi-circles) at 100th cycle than that for a fresh cell (see Fig. 7(d)). The increase in these impedances is also responsible for the increased potential drop during intercalation/deintercalation processes of lithium in the solid matrix and results in loss in discharge capacity of cell with cycling.

Table 5
Various properties of LMO half-cells predicted by simulations at different stages of cycling.

Rate	N	r (μm)	R_{film} (Ωm²)	ε_{diss} (%)	c_s (M) at EOD	c_s (M) at EOC
1C	1	7.989	0.002	0.125	20.345	4.904
	50	7.754	0.020	2.741	20.263	4.949
	100	7.545	0.036	4.942	20.185	4.997
2C	1	7.994	0.001	0.074	17.910	4.903
	50	7.846	0.013	1.737	17.817	4.931
	100	7.702	0.024	3.306	17.723	4.961

The rise in volume fraction of the inactive solid phase and corresponding reduction in the average size of particles of the spinel electrode with cycling at 1C and 2C currents are listed in Table 5. From this tabulated data, a gradual decrease in the particle radius from 8 to 7.55 and 7.70 μm is noticed at 1C and 2C currents, respectively. The lost spinel material is dissolved in electrolyte and deposited as inactive phase which is observed to be 4.94 and 3.30% of the electrode volume for cycling at 1C and 2C currents, respectively. The deposited film on the reaction surface is responsible for the increased cell resistance for the electrochemical reaction in the subsequent cycles. The film resistance increases with cycling and is calculated to be 0.036 and 0.024 Ω-m² at 100th

cycles of 1C and 2C currents, respectively, which results in increased IR losses and leads to lower cell capacity. Since the current passes for a longer duration when cycling at lower currents, the higher film resistance predicted in case of 1C is due to the model (equation (25)) in which the amount of Mn dissolved depends on time ($X_a \sim t^3$).

With reduction in electrode interfacial area and active solid phase, the availability of sites to host lithium also decreases. To examine the change in cyclable lithium with continuous cycling, the space-averaged lithium concentration of the LMO electrode at EOC and EOD of cell cycled at 1C and 2C rates are also given in Table 5. Through comparison of the concentration at EOC and EOD, it can be inferred that the amount of cyclable lithium gradually decreases with increase in cycle number. The amount of lithium is observed to be lower in the case of 2C as compared to 1C current which is expected to be caused by the increased overpotential at high rate operation of cell. This loss in cyclable lithium is also responsible for the reduction in cell capacity with cycling.

Lastly, a comparison of cycling performance at 1C and 2C currents for Li-MCMB, Li-LMO and MCMB-LMO cells is presented in Fig. 8. The first cycle discharge capacities of these cells are 1.56, 1.29 and 1.08 mAh at 1C rate, respectively, with corresponding initial discharge capacities at 2C current of 1.52, 1.08 and 1.003 mAh. From this plot the loss in discharge capacity of these cells when cycled at 1C (2C) rates for 100 cycles are observed to be 37.79 (46.40), 16.5 (22.0) and 23.5 (37.5) % of the initial capacities, respectively. From this comparison it is evident that MCMB electrode has a faster rate of capacity loss at both currents as compared to the LMO electrode which elucidate that the former electrode plays a dominant role in the degradation of the full-cells with cycling.

It should be emphasized that the degradation is considered to be due to consumption of lithium in forming a carbonate layer on the surface of active material in MCMB half-cells cycled in this work, whereas in LMO it is attributed to dissolution and the corresponding loss of a lithium storage site. In this study, it is observed that the inactive solid phase originating from the disproportionation reaction (i.e., Mn^{+4}) and that is deposited on the active material increases the resistance and causes loss in discharge capacity of the LMO cathode. The rate of degradation, as suggested by Wang et al. [51], is also dependent on the amount of cyclable lithium available in the cell. In the case of MCMB-LMO cells, the cyclable lithium is limited by the amount of lithium stored in the spinel cathode.

In this work, the 1C rate of full-cells is defined based on the capacity of the limiting electrode, which being the LMO electrode. That is, the 1C and 2C currents have been determined based on the material loading of the LMO electrodes. In MCMB-LMO full-cells the working voltage range has been chosen to be 3.0-4.2 V to avoid deep-discharge and over-charge effects. With this scenario, the voltage window for testing of capacity degradation of MCMB half-cells has been assumed to be 0.005–2 V that corresponds to complete utilization of this material. Further, it should be noted that the ratio of capacities of MCMB and LMO electrodes in the present work is greater than 1. As a result, when cycled at the nominal 1C current of MCMB-LMO full-cells, Li-MCMB half-cells undergo electrochemical and parasitic reactions for a longer time duration that is also corroborated by our simulations (though not shown, a longer charging duration has been observed). It is expected that these reasons lead to the formation of a thicker SEI and faster capacity loss in case of Li-MCMB half-cells as compared to MCMB-LMO full-cells.

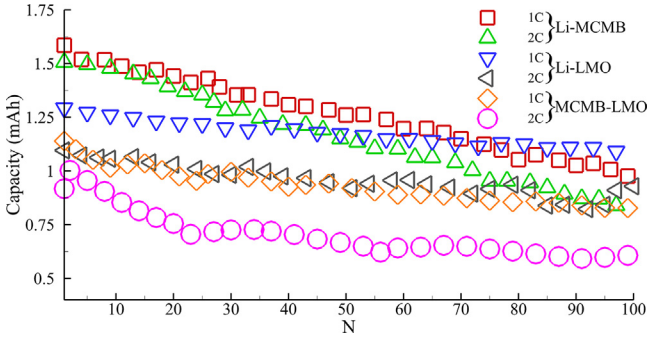

Fig. 8. A comparison of discharge capacities vs. cycle number obtained through experiments on Li-MCMB, Li-LMO and MCMB-LMO cells at 1C and 2C rates.

5. CONCLUSIONS

In this work, electrochemical performance assessment of MCMB and LMO electrodes in 2016-type coin cells were performed through cyclic voltammogram, electrochemical impedance spectroscopy and galvanostatic cycling techniques. Through galvanostatic cycling, the capacity fade in MCMB-LMO cells was observed to be 23.5% and 37.5% of initial capacity in 100 cycles at 1C and 2C-rates, respectively. An increase in cell impedance with increase in cycle number was observed and was attributed to the deposition of inactive solid phase over the surface of the electrodes. An examination of the surface morphology of the fresh and cycled electrode revealed that the electrode texture was modified due to the SEI film formation at anode and manganese dissolution with inactive solid deposition at LMO electrode.

The loss in discharge capacity of Li-ion cells is a cumulative effect of degradation of cathode and anode and the electrode which has dominant role in capacity fade is hard to identify. The contribution of each electrode in capacity loss of full-cells was ascertained by the performance assessment of MCMB and LMO half-cells. Experiments revealed that the fabricated half-cells when discharged for 100 cycles at 1C rate led to 37.79% and 16.5% loss in initial capacity for MCMB and LMO, respectively, which signifies that the former has a higher contribution in the degradation of discharge capacity in the full-cell format. Analogous to full-cells, an increased loss in capacity is also observed at 2C current in case of both half-cells due to kinetic limitations and ohmic resistances. The lithium diffusion coefficient dictates the rate of intercalation/deintercalation in the solid phase of the MCMB and LMO electrodes. Lithium diffusion coefficient in the solid matrix at different state of lithiation of MCMB and LMO half-cells were also determined and was found to vary between 1.95×10^{-16} to 3.98×10^{-13} m^2/s and 9.15×10^{-15} to 2.27×10^{-13} m^2/s for MCMB and LMO electrodes, respectively. The diffusivity together with other measured parameters have been further used as inputs in numerical simulations of MCMB and LMO half-cells.

The capacity loss in MCMB and LMO half-cells was investigated though an experimentally validated numerical model. MCMB half-cells were modeled by considering electrolyte reduction as a parasitic reaction, while in LMO half-cells manganese dissolution was used to capture the degradation in discharge capacity with cycling. The simulated results of MCMB shows that the film resistance and loss in electrode porosity increase with cycling, which leads to loss in cell capacity. The loss in cyclable lithium with increase in cycle number is also responsible for the degradation of MCMB electrodes. In case of LMO half-cells simulations, the loss in discharge capacity is quantified to be caused by the reduction in active material and increase in surface resistance with cycling. The half-cell models can be further employed for estimation of degradation parameters, cycle life and causes of failure of MCMB and LMO electrodes. The microstructural crack formation and corresponding change in tortuosity in the MCMB and LMO

electrodes was not considered in this work to manage the complexity of the numerical model. However, there is a possibility of increasing tortuosity in the material due to cracking and variation in surface film which may also influence capacity fading in full-cells. The authors consider this aspect to be a challenging problem, characterization and quantification of which may emerge as a potential direction for further research.

ACKNOWLEDGMENT

The authors would like to acknowledge the financial support received from the Department of Science and Technology (DST) under SERC/ET-0129/2012 and Council of Scientific & Industrial Research (CSIR) under 22/648/13/EMR-II. The authors would also to like to thank Surface Characterization Lab, IIT Kanpur for time on the XPS instrument. The assistance of Mr. Salahuddin Ahamad in conducting experiments and numerical analysis of the data is also acknowledged.

Appendix A. Supplementary data

Supplementary data associated with this article can be found, in the online version, at http://dx.doi.org/10.1016/j.electacta.2017.02.040.

References

[1] G.A. Nazri, G. Pistoia, Lithium Batteries Science and Technology, first ed., Springer, New York, 2009.
[2] M. Yoshio, R.J. Brodd, A. Kozawa, Lithium-Ion Batteries: Science and Technologies, first ed., Springer, New York, 2009.
[3] U.K. Sen, S. Mitra, Improved electrode fabrication method to enhance performance and stability of MoS_2-based Li-ion battery anode, J. Sol. State. Electroch 18 (2014) 2701–2708.
[4] L. Bazin, S. Mitra, P.L. Taberna, P. Poizot, M. Gressier, M.J. Menu, A. Barnabé, P. Simon, J.M. Tarascon, High rate capability pure Sn-based nano-architectured electrode assembly for rechargeable lithium batteries, J. Power Sources 188 (2009) 578–582.
[5] A. Bhaskar, M. Deepa, T.N. Rao, U.V. Varadaraju, Enhanced nanoscale conduction capability of a MoO_2/Graphene composite for high performance anodes in lithium ion batteries, J. Power Sources 216 (2012) 169–179.
[6] C. Julien, A. Mauger, A. Vijh, K. Zaghib, Lithium Batteries: Science and Technology, first ed., Springer, New York, 2016.
[7] S. Flandrois, B. Simon, Carbon materials for lithium-ion rechargeable batteries, Carbon 37 (1999) 165–180.
[8] S. Hossain, Y.K. Kim, Y. Saleh, R. Loutfy, Comparative studies of MCMB and C-C composite as anodes for lithium-ion battery systems, J. Power Sources 114 (2003) 264–276.
[9] P. Arora, R.E. White, S. Carolina, M. Doyle, Capacity fade mechanisms and side reactions in Li-ion batteries, J. Electrochem. Soc. 145 (1998) 3647–3667.
[10] G.L. Plett, Algebraic solution for modeling SEI layer growth, ECS Electrochem. Lett. 2 (2013) A63–A65.
[11] J.S. Kim, Y.T. Park, Characteristics of surface films formed at a mesocarbon microbead electrode in a Li-ion battery, J. Power Sources 91 (2000) 172–176.
[12] M.M. Thackeray, P.J. Johnson, L.A.D. Picciotto, P.G. Bruce, J.B. Goodenough, Electrochemical extraction of lithium from $LiMn_2O_4$, Mat. Res. Bulletin 19 (1984) 179–187.
[13] O.K. Park, Y. Cho, S. Lee, H.-C. Yoo, H.-K. Song, J. Cho, Who will drive electric vehicles, olivine or spinel? Energy & Environm. Sci. 4 (2011) 1621–1633.
[14] S.B. Chikkannanavar, D.M. Bernardi, L. Liu, A review of blended cathode materials for use in Li-ion batteries, J. Power Sources 248 (2014) 91–100.
[15] J.H. Seo, J. Park, G. Plett, A.M. Sastry, Gas-evolution induced volume fraction changes and their effect on the performance degradation of Li-ion batteries, Electrochem. Sol. State Lett. 13 (2010) A135–A137.
[16] Y. Dai, L. Cai, R.E. White, Capacity fade model for spinel $LiMn_2O_4$ electrode, J. Electrochem. Soc. 160 (2013) A182–A190.
[17] X. Lin, J. Park, L. Liu, Y. Lee, A.M. Sastry, W. Lu, A comprehensive capacity fade model and analysis for Li-ion batteries, J. Electrochem. Soc. 160 (2013) A1701–A1710.
[18] J. Shin, C. Han, U. Jung, S. Lee, Effect of Li_2CO_3 additive on gas generation in lithium-ion batteries, J. Power Sources 109 (2002) 47–52.
[19] G. Sikha, R.E. White, Effect of porosity on the capacity fade of a Li-ion battery: theory, J. Electrochem. Soc. 151 (2004) 1104–1114.
[20] P. Ramadass, B. Haran, R. White, B.N. Popov, Capacity fade of Sony 18650 cells cycled at elevated temperatures Part I: Cycling performance, J. Power Sources 112 (2002) 606–613.
[21] P. Ramadass, B. Haran, R. White, B.N. Popov, Capacity fade of Sony 18650 cells cycled at elevated temperatures Part II: Capacity fade analysis, J. Power Sources 112 (2002) 614–620.
[22] P. Ramadass, B. Haran, P.M. Gomadam, R. White, B.N. Popov, Development of first principles capacity fade model for Li-ion cells, J. Electrochem. Soc. 151 (2004) A196–A203.
[23] T. Yoshida, M. Takahashi, S. Morikawa, C. Ihara, H. Katsukawa, T. Shiratsuchi, J. Yamaki, Degradation mechanism and life prediction of Li-ion batteries, J. Electrochem. Soc. 153 (2006) A576–A582.
[24] V.R. Subramanian, V. Boovaragavan, V. Ramadesigan, M. Arabandi, Mathematical model reformulation for Li-ion battery simulations: galvanostatic boundary conditions, J. Electrochem. Soc. 156 (2009) A260–A271.
[25] V. Ramadesigan, K. Chen, N.A. Burns, V. Boovaragavan, R.D. Braatz, V.R. Subramanian, Parameter estimation and capacity fade analysis of Li-ion batteries using reformulated models, J. Electrochem. Soc. 158 (2011) A1048–A1054.
[26] G. Ning, R.E. White, B.N. Popov, A generalized cycle life model of rechargeable Li-ion batteries, Electrochim. Acta 51 (2006) 2012–2022.
[27] M. Rashid, A. Gupta, Mathematical model for combined effect of SEI formation and gas evolution in Li-ion batteries, ECS Electrochem. Lett. 3 (2014) A95–A98.
[28] C.H. Lu, S.W. Lin, Dissolution kinetics of spinel lithium manganate and its relation to capacity fading in Li-ion batteries, J. Mat. Research 17 (2002) 1476–1481.
[29] J. Park, J.H. Seo, G. Plett, W. Lu, A.M. Sastry, Numerical simulation of the effect of the dissolution of $LiMn_2O_4$ particles on li-ion battery performance, Electrochem. Sol. State Lett. 14 (2011) A14–A18.
[30] L. Cai, Y. Dai, M. Nicholson, R.E. White, K. Jagannathan, G. Bhatia, Life modeling of a lithium ion cell with a spinel-based cathode, J. Power Sources 221 (2012) 191–200.
[31] M. Doyle, T.F. Fuller, J. Newman, Modeling of galvanostatic charge and discharge of the lithium/polymer/insertion cell, J. Electrochem. Soc 140 (1993) 1526–1533.
[32] T.F. Fuller, M. Doyle, J. Newman, Simulation and optimization of the dual Li-ion insertion cell, J. Electrochem. Soc. 141 (1994) 1–10.
[33] M. Doyle, J. Newman, A.S. Gozdz, C.N. Schmutz, J.M. Tarascon, Comparison of modeling predictions with experimental data from plastic Li-ion cells, J. Electrochem. Soc 143 (1996) 1890–1903.
[34] M. Rashid, A. Gupta, Effect of relaxation periods over cycling performance of a Li-ion battery, J. Electrochem. Soc. 162 (2015) A3145–A3153.
[35] W. Weppner, A. Huggins, Determination of the kinetic parameters of mixed-conducting electrodes and application to the system Li_3Sb, J. Electrochem. Soc. 124 (1977) 1569–1577.
[36] G.L. Plett, Battery management systems, Battery modeling, Vol 1, Artech House, Norwood, 2015.
[37] A. Gupta, J.H. Seo, X. Zhang, W. Du, A.M. Sastry, W. Shyy, Effective transport properties of $LiMn_2O_4$ electrode via particle-scale modeling, J. Electrochem. Soc. 158 (2011) A487–A497.
[38] J. Yao, G.X. Wang, J.H. Ahn, H.K. Liu, S.X. Dou, Electrochemical studies of graphitized mesocarbon microbeads as an anode in lithium-ion cells, J. Power Sources 114 (2003) 292–297.
[39] S. Yang, H. Song, X. Chen, Electrochemical performance of expanded mesocarbon microbeads as anode material for lithium-ion batteries, Electrochem. Commun 8 (2006) 137–142.
[40] R.P. Ramasamy, J.W. Lee, B.N. Popov, Simulation of capacity loss in carbon electrode for lithium-ion cells during storage, J. Power Sources 166 (2007) 266–272.
[41] M. Tang, A. Yuan, J. Xu, Synthesis of highly crystalline $LiMn_2O_4$/multiwalled carbon nanotube composite material with high performance as lithium-ion battery cathode via an improved two-step approach, Electrochim. Acta 166 (2015) 244–252.
[42] L. Xiao, Y. Guo, D. Qu, B. Deng, H. Liu, D. Tang, Influence of particle sizes and morphologies on the electrochemical performances of spinel $LiMn_2O_4$ cathode materials, J. Power Sources 225 (2013) 286–292.
[43] Xiamen TOB New Energy Technology Co., http://www.tobmachine.com/ (accessed on 16th May 2016).
[44] X. Li, Y. Xu, C. Wang, Novel approach to preparation of $LiMn_2O_4$ core/$LiNi_xMn_{2-x}O_4$ shell composite, A. Surface Science 255 (2009) 5651–5655.
[45] Y. Liu, X. Li, H. Guo, Z. Wang, Q. Hu, W. Peng, Y. Yang, Electrochemical performance and capacity fading reason of $LiMn_2O_4$/graphite batteries stored at room temperature, J. Power Sources 189 (2009) 721–725.
[46] P. Liu, Diffusion of lithium in carbon, Solid State Ionics 92 (1996) 91–97.
[47] C. Julien, E.H. Poniatowski, M.A.C. Lopez, L.E. Alarcon, J.J. Jarquin, Growth of $LiMn_2O_4$ thin films by pulsed-laser deposition and their electrochemical properties in lithium microbatteries, Mat. Sci. Engg. B: Solid-State Mat. Advan. Tech. 72 (2000) 36–46.
[48] J. Xie, K. Kohno, T. Matsumura, N. Imanishi, A. Hirano, Y. Takeda, O. Yamamoto, Li-ion diffusion kinetics in $LiMn_2O_4$ thin films prepared by pulsed laser deposition, Electrochim. Acta 54 (2008) 376–381.
[49] C. Delacourt, M. Ati, J.M. Tarascon, Measurement of lithium diffusion coefficient in Li_yFeSO_4F, J. Electrochem. Soc. 158 (2011) A741–A749.
[50] J. Xie, T. Tanaka, N. Imanishi, T. Matsumura, A. Hirano, Y. Takeda, O. Yamamoto, Li-ion transport kinetics in $LiMn_2O_4$ thin films prepared by radio frequency magnetron sputtering, J. Power Sources 180 (2008) 576–581.
[51] E. Wang, D. Ofer, W. Bowden, N. Iltchev, R. Moses, K. Brandt, Stability of Lithium Ion Spinel Cells: III. Improved life of charged cells, J. Electrochem. Soc 147 (2000) 4023–4028.